Electronic Supplementary Material (ESI) for Nanoscale.

Designed synthesis of nickel-cobalt-based electrode materials for high-performance solid-state hybrid supercapacitors

Liu Yang[a], Xintong Lu[a], Shihao Wang[a], Jiansen Wang[a], Xiaohui Guan[a]*, Xin Guan[b]* and Guangsheng Wang[c]*

[a] *School of Chemical Engineering, Northeast Electric Power University, Jilin 132000, PR China. guanxh@neepu.edu.cn*

[b] *Physics Department, Lancaster University, United Kingdom. x.guan2@lancaster.ac.uk*

[c] *Key Laboratory of Bio-Inspired Smart Interfacial Science and Technology of Ministry of Education, School of Chemistry and Environment, Beihang University, Beijing 100191, PR China. wanggsh@buaa.edu.cn*

*Corresponding authors: Tel. /fax: 86-0432-64807377

E-mail: guanxh@neepu.edu.cn (Xiaohui Guan)

Contents

1. Material synthesis

1.1 Synthesis of the Ni-Co-Cu oxalate precursor

The preparation of the Ni-Co-Cu-based oxalate precursor was similar to that of the $Ni(Co)C_2O_4{\cdot}2H_2O$ precursor, applying a complexation reaction, which also could achieve the mass production. Typically, 2 mmol of $Ni(NO_3)_2{\cdot}6H_2O$, 0.5 mmol of $Co(NO_3)_2{\cdot}6H_2O$ and 0.1 mmol of $Cu(NO_3)_2{\cdot}3H_2O$ were dissolved in 80 mL of ultrapure water under constant magnetic stirring, then 6 mmol of $H_2C_2O_4{\cdot}2H_2O$ was added into the former solution, and the complexation reaction shortly occurred, with the generation of light green products. After stirring for 8 h at room temperature, the final product was collected by centrifugation and rinsed with ultrapure water and ethanol for several times to eliminate the impurities, and finally dried at 50 ℃ for 12 h.

1.2 Synthesis of the Ni-Co-Cu ternary hydroxide

First of all, 0.1 g of the Ni-Co-Cu oxalate precursor and 0.24 g of sodium hydroxide (NaOH) were homogeneously dispersed in 30 mL of ultrapure water under magnetic stirring, respectively. Then the NaOH solution was poured into the first one, and the color of the solution slowly changed into light green. After stirring at room temperature for 12 h, the green product was collected by centrifugation, rinsed with ultrapure water and ethanol for several times, and finally dried at 50 ℃ overnight.

1.3 Synthesis of the $Cu(Ni, Co)_2S_4$

In a typical process, 0.1 g of Ni-Co-Cu oxalate precursor and 1.2 g of $Na_2S{\cdot}9H_2O$ were uniformly dispersed in 30 mL of ultrapure water under magnetic stirring, respectively. Afterwards, the $Na_2S{\cdot}9H_2O$ solution was added into the first one as S^{2-} source, and the color of the solution gradually changed into dark black. Then the mixture was stirred at room temperature for 1 h, and loaded in a 100 mL Teflon-lined stainless steel autoclave, maintaining at 120 ℃ for 8 h. After air cooling to room temperature, the final product was collected by centrifugation and rinsed with ultrapure water and ethanol for several times to eliminate the impurities, and ultimately dried at 50 ℃ overnight.

1.4 Synthesis of the BC

The S-P-Ca-Zn-Fe-doped biomass-derived carbon (BC) was prepared using eggplant as the carbon source. Firstly, the eggplant was cleaned with ultrapure water for several times, cut in pieces and dried at 80 ℃ for 5 days. Then the dried eggplant was adequately ground to fine powder. Finally, the eggplant powder was annealed in N_2 at 700 ℃ for 2 h, with a heating rate of 2 ℃ min^{-1}.

2. SEM characterization of the $CoNi_2S_4$ obtained at different S^{2-} contents

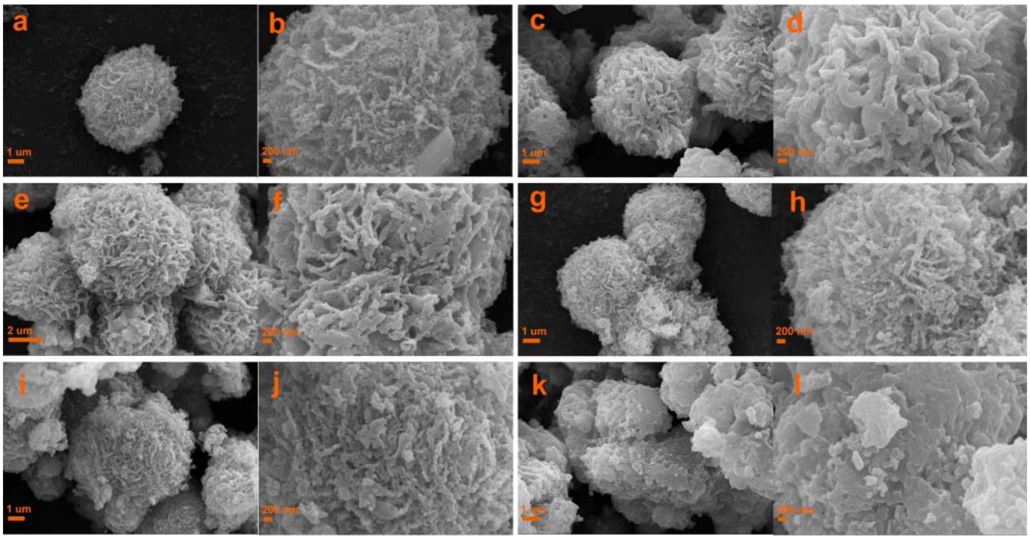

Fig. S1. SEM images of $CoNi_2S_4$ obtained at different S^{2-} contents: 2 mmol (a and b); 4 mmol (c and d); 6 mmol (e and f); 8 mmol (g and h); 10 mmol (i and j); 12 mmol (k and l).

As shown in Fig. S1, apparently, at relatively lower S^{2-} content ($n_{Na_2S\cdot 9H_2O}$ = 2 mmol), the nanosheets on the surface of the $CoNi_2S_4$ became rougher than those of the $Ni(Co)C_2O_4\cdot 2H_2O$ precursor, but the microflower structure was retained, which could also provide large interactive surface area between the electrode and the electrolyte, arising more Faradic redox reactions (Fig. S1a ~ b). As the S^{2-} content increased to 4, 6 and 8 mmol, the nanosheet structure suffered from severe collapsion, resulting in small-sized thicker layers irregularly wrapping outside the microstructure of the $CoNi_2S_4$ (Fig. S1c ~ h). When the S^{2-} content was tuned to 10 and 12 mmol, the whole microflower-like structure was wrecked by the high anion exchange rate, and the nanosheet structure totally disappeared, being replaced by numerous agglomerated particles (Fig. S1i ~ l). Based on the SEM results, it was clear that as the S^{2-} content increased, the morphology and structure of $CoNi_2S_4$ experienced more damage, especially the vulnerable nanosheet structure, however, the basic microsphere structure of the precursor could be inherited, which was robust enough to endure the high anion exchange rate.

3. XRD characterization of the $Ni(Co)C_2O_4{\cdot}2H_2O$, $CoNi_2S_4$ and NiCo-LDH obtained under different conditions

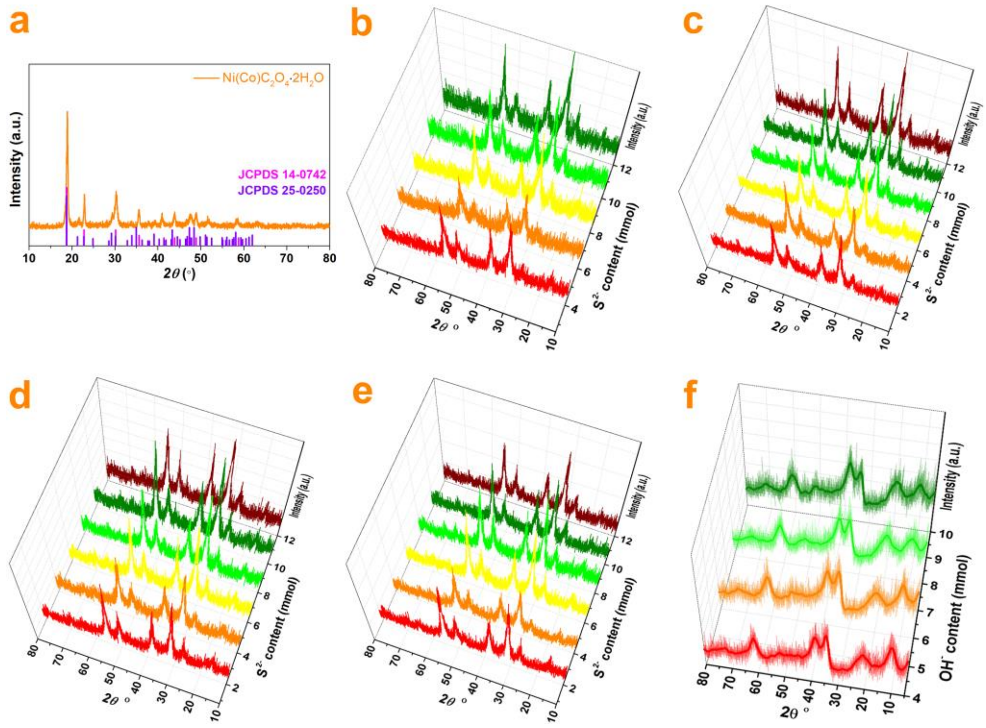

Fig. S2. XRD pattern of $Ni(Co)C_2O_4{\cdot}2H_2O$ (a). XRD patterns of $CoNi_2S_4$ obtained under different reaction time with various S^{2-} contents: 4 h (b); 12 h (c); 16 h (d); 20 h (e). XRD patterns of the NiCo-LDH obtained at different OH^- contents (f).

The XRD measurements for the $CoNi_2S_4$ and NiCo-LDH obtained at different synthesis conditions were carried out to confirm the composition and phase structure. The XRD patterns for the $CoNi_2S_4$ materials obtained with the S^{2-} content ranging from 2 mmol to 12 mmol, and the sulfidation reaction time changing from 4 h to 20 h, were shown in Fig. S2b ~ e. It could be clearly seen that all the XRD patterns followed the same crystalline structure characteristics of the cubic phase $CoNi_2S_4$ (JCPDS 24-0334), with sharp diffraction peaks and nearly no other interfering peaks. The XRD pattern for the material produced at the S^{2-} content of 2 mmol and reaction time of 4 h was not placed in Fig. S2b, due to the existence of several undesired peaks, resulting from the incomplete sulfidation of the precursor. Thus, when the reaction time was not long enough, the concentration of the S^{2-} should be appropriately raised to increase the reaction rate and generate the pure phase products. Since the NiCo-LDH nanomaterials were prepared at room temperature, OH^- content was the only factor that concerned during the synthesis process in this work, and the XRD characterization results were shown in Fig. S2f. All the XRD patterns were of similar characteristics, with identical peaks appearing at the same 2θ degree, which were all in accordance with the Ni-Co-based layered double hydroxide (NiCo-LDH) reported previously.[43]

4. N_2 adsorption-desorption measurements of the $Ni(Co)C_2O_4{\cdot}2H_2O$ and NiO/Co_3O_4

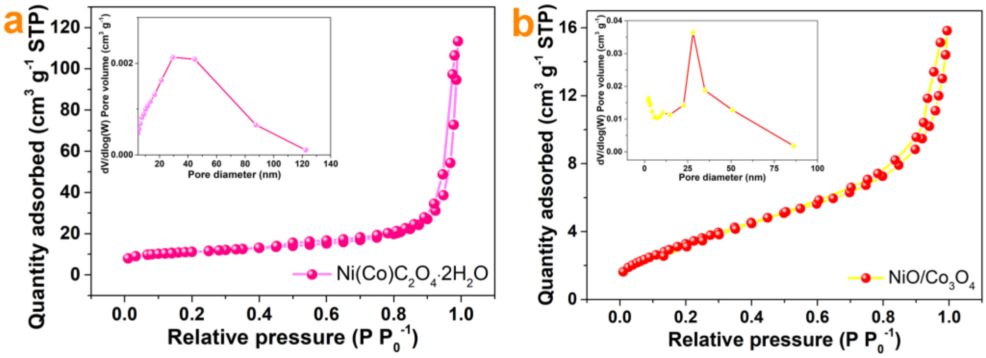

Fig. S3. N_2 adsorption-desorption isotherm loop and BJH pore-size distribution (inset) for $Ni(Co)C_2O_4{\cdot}2H_2O$ (a); NiO/Co_3O_4 (b).

5. Electrochemical performance of the NiCo-LDH and NiO/Co_3O_4

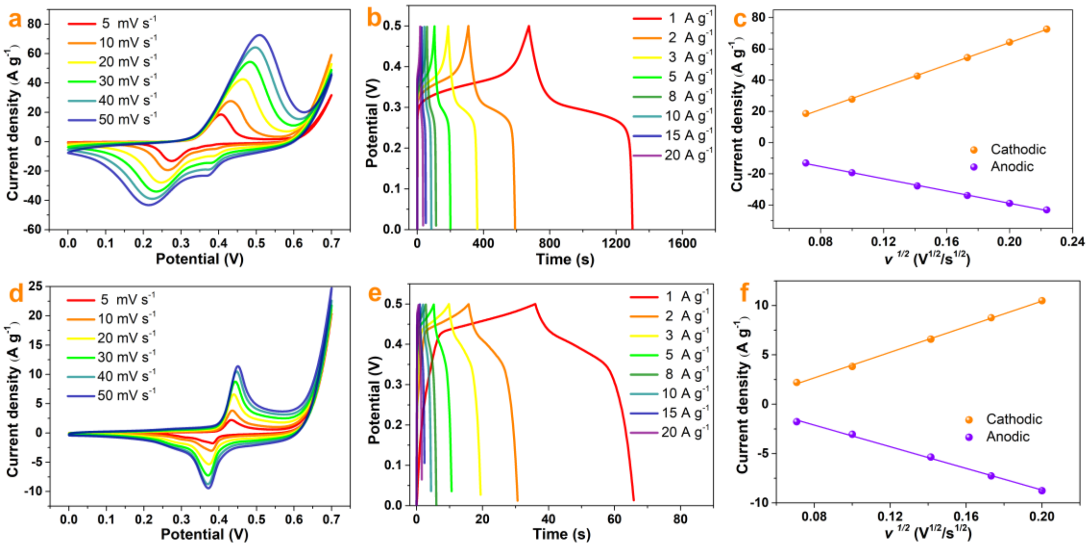

Fig. S4. CV curves of NiCo-LDH at various scan rates of 5 ~ 50 mV s^{-1} (a); GCD curves of NiCo-LDH at different current densities of 1 ~ 20 A g^{-1} (b); the linear relation between the anodic/cathodic peak currents and the square root of scan rates for NiCo-LDH (c); CV curves of NiO/Co_3O_4 at various scan rates of 5 ~ 50 mV s^{-1} (d); GCD curves of NiO/Co_3O_4 at different current densities of 1 ~ 20 A g^{-1} (e); the linear relation between the anodic/cathodic peak currents and the square root of scan rates for NiO/Co_3O_4 (f).

6. GCD tests of the $CoNi_2S_4$ prepared under different conditions

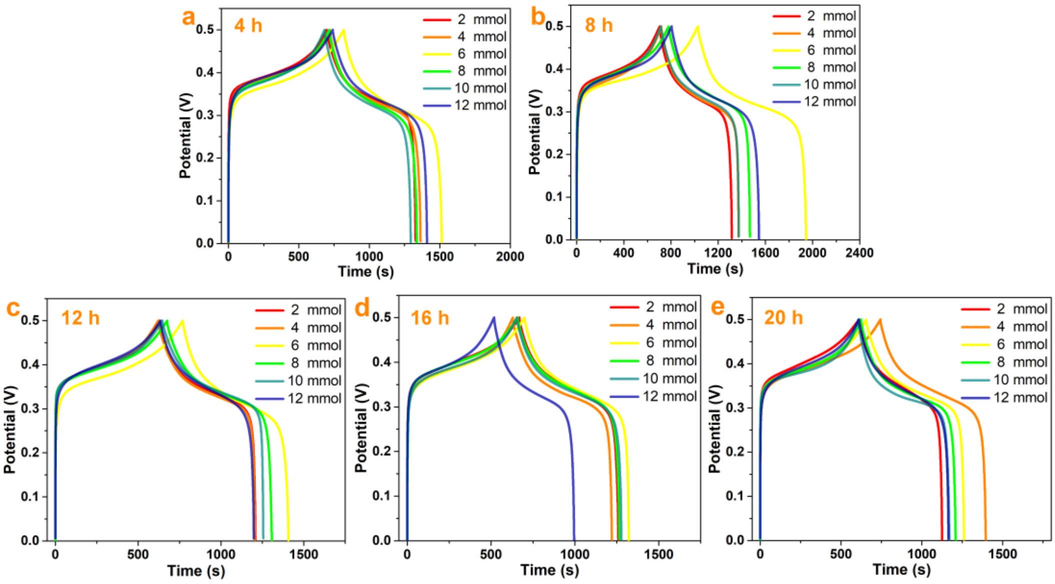

Fig. S5. GCD curves of $CoNi_2S_4$ prepared under different reaction time with various S^{2-} contents (1 A g^{-1}): 4 h (a); 8 h (b); 12 h (c); 16 h (d); 20 h (e).

7. Electrochemical performance of the NiCo-LDH obtained at different OH$^-$ contents

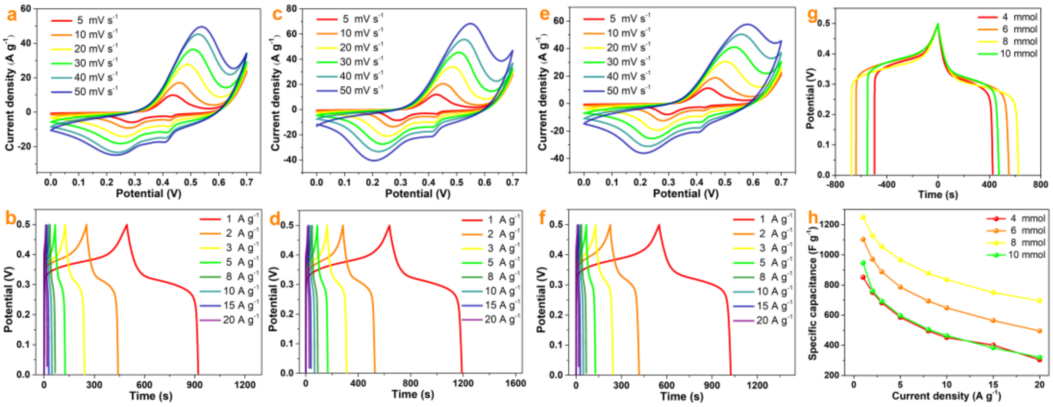

Fig. S6. CV curves of NiCo-LDH obtained at different OH$^-$ contents at various scan rates of 5 ~ 50 mV s^{-1}: 4 mmol (a); 6 mmol (c); 10 mmol (e). GCD curves of NiCo-LDH obtained at different OH$^-$ contents at different current densities of 1 ~ 20 A g^{-1}: 4 mmol (b); 6 mmol (d); 10 mmol (f). GCD curves of NiCo-LDH obtained at different OH$^-$ contents at a current density of 1 A g^{-1} (g). The specific capacitance of NiCo-LDH obtained at different OH$^-$ contents versus different current densities (h).

8. Cycling stability tests of the Cu(Ni, Co)$_2$S$_4$ and Ni-Co-Cu ternary hydroxide

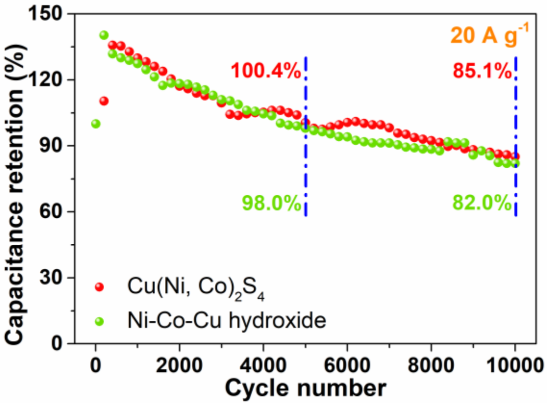

Fig. S7. Cycling performance of the Cu(Ni, Co)$_2$S$_4$ and Ni-Co-Cu ternary hydroxide at a current density of 20 A g^{-1}.

9. Cycling stability test of the BC

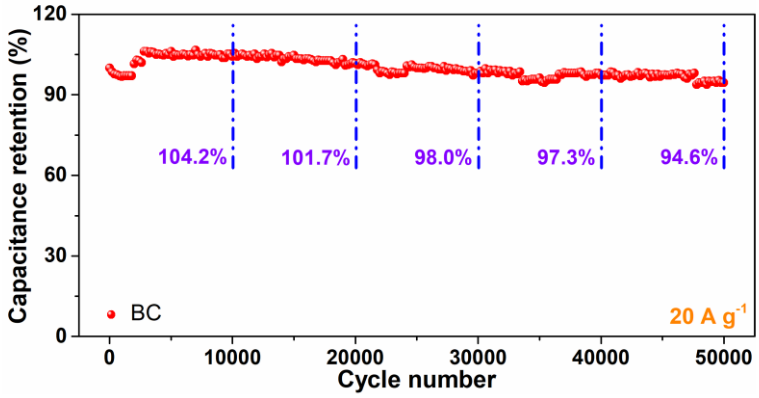

Fig. S8. Cycling performance of the BC at a current density of 20 A g^{-1}.

10. SEM results of the materials after cycling tests

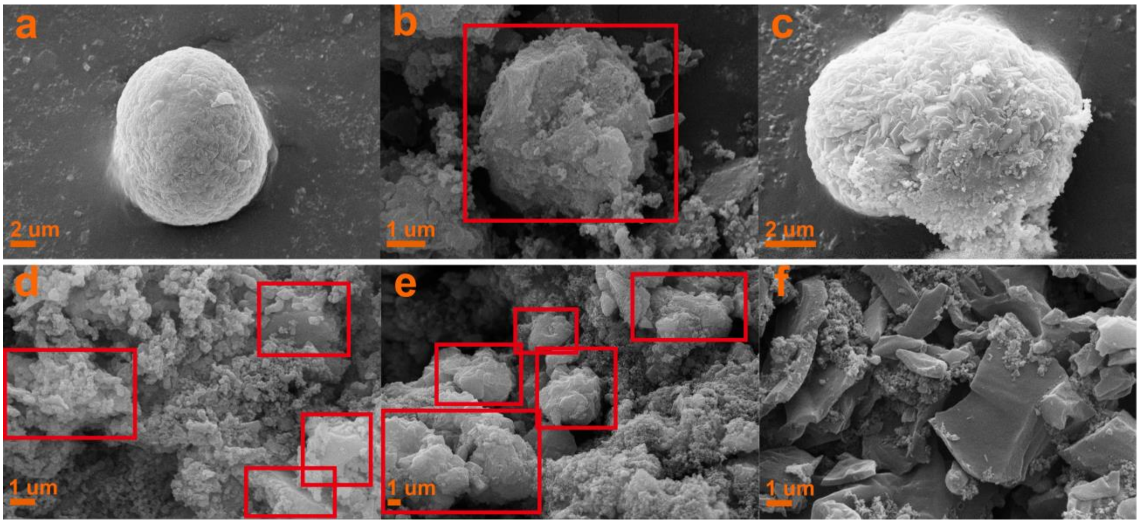

Fig. S9. SEM images of the materials after cycling tests: $CoNi_2S_4$ (a); NiCo-LDH (b); NiO/Co_3O_4 (c); $Cu(Ni, Co)_2S_4$ (d); Ni-Co-Cu ternary hydroxide (e); BC (f).

SEM characterization was carried out to investigate the morphology and structure of the materials after the cycling test, and the SEM images of the $CoNi_2S_4$, NiCo-LDH, NiO/Co_3O_4, $Cu(Ni, Co)_2S_4$, Ni-Co-Cu ternary hydroxide and the eggplant-derived heteroatom-doped carbon material (BC) were shown in Fig. S9. The basic morphology and structure of $CoNi_2S_4$, NiCo-LDH and NiO/Co_3O_4 was microsphere, and it was obvious that the basic structure of the three materials did not change greatly after cycling for 10000 cycles. However, the nanolayers coated on the surface of the $CoNi_2S_4$ disappear, and so does the nanosheet structure outside the NiCo-LDH and NiO/Co_3O_4 materials. After long-term cycles, the fragile layer structure suffers from great damage and collapsion, and the specific surface areas of the materials decrease a lot, which has a negative influence on the efficient contact between the active material and the electrolyte, and consequently results in the decline of the specific capacitance during the long-term cycling. But the main basic microsphere structure is maintained, which is favorable for the cycling stability of the materials. The $Cu(Ni, Co)_2S_4$ and Ni-Co-Cu ternary hydroxide are still of the bulk structure after cycling for 10000 times. The morphology and structure of

BC almost remain the same, mainly because of the robust structure of the material and the electric double-layer capacitive behavior without the occurrence of chemical reactions, which may explain the superior long-term cycling stability of the material. Because the working electrode is fabricated by mixed acetylene black, PTFE and prepared materials, which are difficult to separate, thus, there are some impurities (acetylene black and PTFE) existing in the SEM images.

11. Table of the specific capacitance for the $CoNi_2S_4$ and NiCo-LDH prepared under different conditions

Table S1. The specific capacitance (at 1 A g^{-1}) of the $CoNi_2S_4$ prepared at different reaction time with various S^{2-} contents.

Reaction time (h)	**Specific capacitance (F g^{-1})**					
	$Na_2S·9H_2O$ content (mmol)					
	2	**4**	**6**	**8**	**10**	**12**
4	1262.8	1287.2	1391.8	1244.2	1222.4	1336.1
8	1222.6	1310.9	1836.6	1376.9	1321.3	1482.2
12	1163.9	1166.7	1277.3	1264.0	1218.4	1128.7
16	1182.6	1181.6	1246.0	1216.0	1247.2	953.7
20	1028.6	1303.3	1211.6	1170.3	1126.3	1107.1

Table S2. The specific capacitance of the NiCo-LDH prepared with various OH^- contents.

NaOH content (mmol)	**Specific capacitance (F g^{-1})**							
	Current density (A g^{-1})							
	1	**2**	**3**	**5**	**8**	**10**	**15**	**20**
4	850.6	751.2	681.6	586.0	496.0	452.0	402.0	304.0
6	1102.9	970.5	886.8	786.0	694.4	648.0	564.0	496.0
8	1249.3	1126.5	1054.8	966.0	876.8	836.0	750.0	696.0
10	947.0	760.8	692.4	598.0	505.6	464.0	384.0	320.0

12. Table of the electrochemical performance comparisons of the CoNi$_2$S$_4$ and previous reports

Table S3. Comparisons of the electrochemical performance of the CoNi$_2$S$_4$ with previous reports.

Material	Capacitance	Current density	Cycling performance	Energy density	Power density	Cycling stability of the device	Reference
NiCo$_2$S$_4$/graphene	1432 F g^{-1}	1 A g^{-1}	--	43.4 Wh kg^{-1}	254.3 W kg^{-1}	83.4%, 5000 cycles	54
NiS/NHCS	1150 F g^{-1}	1 A g^{-1}	76%, 4000 cycles	38.3 Wh kg^{-1}	160 W kg^{-1}	96%, 5000 cycles	55
rGO/CoNiS$_x$/N-C	1028.2 F g^{-1}	1 A g^{-1}	93.6%, 2000 cycles	32.9 Wh kg^{-1}	229.2 W kg^{-1}	96.2%, 1500 cycles	56
Ni$_x$Co$_{3-x}$O$_4$/CNTs	668 F g^{-1}	1 A g^{-1}	91.2%, 3500 cycles	23.56 Wh kg^{-1}	800.2 W kg^{-1}	93.75%, 3000 cycles	57
NiCo$_2$S$_4$	972 F g^{-1}	2 A g^{-1}	107.9%, 1000 cycles	28.3 Wh kg^{-1}	245 W kg^{-1}	91.7%, 5000 cycles	58
NiCo$_2$S$_4$@ppy	9.781 F cm^{-2}	0.5 mA cm^{-2}	72.19%, 3000 cycles	34.62 Wh kg^{-1}	120.19 W kg^{-1}	80.64%, 2500 cycles	59
Ni-Co-S@N-pCNFs	520.2 F g^{-1}	0.2 A g^{-1}	--	21.6 Wh kg^{-1}	134.9 W kg^{-1}	90.0%, 3000 cycles	60
NiCo$_2$O$_4$	1229 F g^{-1}	1 A g^{-1}	86.3%, 3000 cycles	21.5 Wh kg^{-1}	750 W kg^{-1}	87.8%, 2000 cycles	61
NiCo$_2$S$_4$/PRGO	1090 F g^{-1}	2 A g^{-1}	80.1%, 3000 cycles	27.5 Wh kg^{-1}	446.5 W kg^{-1}	79.4%, 5000 cycles	62
NiCo$_2$S$_4$/N-graphene	1240 F g^{-1}	1 A g^{-1}	80%, 5000 cycles	36.8 Wh kg^{-1}	375 W kg^{-1}	92%, 3000 cycles	63
CoNi$_2$S$_4$	1836.6 F g^{-1}	1 A g^{-1}	90.5%, 5000 cycles	35.8 Wh kg^{-1}	800.0 W kg^{-1}	132.3%, 50000 cycles	This work
				38.9 Wh kg^{-1}	850.0 W kg^{-1}	101.2%, 50000 cycles	This work